ACS APPLIED NANO MATERIALS

www.acsanm.org

Article

Enhanced Thermoelectric Performance of Nanostructured Cu_2SnS_3 (CTS) via Ag Doping

Ketan Lohani, Himanshu Nautiyal, Narges Ataollahi, Umberto Anselmi-Tamburini, Carlo Fanciulli, and Paolo Scardi*

Cite This: *ACS Appl. Nano Mater.* 2023, 6, 6323–6333

Read Online

ACCESS | Metrics & More | Article Recommendations | Supporting Information

ABSTRACT: The present work aims to investigate the effect of Ag doping on the thermoelectric properties of Cu_2SnS_3 (CTS). Various $Cu_2Ag_{(x)}Sn_{(1-x)}S_3$ ($0.05 \leq x \leq 0.25$) samples were synthesized by mechanical alloying followed by spark plasma sintering, and their structural and transport properties were systematically investigated. The $x = 0.15$ sample presented a ~10-fold higher power factor than the undoped CTS. Although, the $x = 0.125$ sample had a lower power factor than the $x = 0.15$ sample, owing to its lower thermal conductivity, both the samples showed the highest zT ~ 0.8 at 723 K. This value is comparable to the best results available in the literature for earth-abundant and eco-friendly thermoelectric materials. Interestingly, the thermal conductivity of $Cu_2Ag_{(x)}Sn_{(1-x)}S_3$ samples increased with Ag substitution, which was further investigated using the first-principles and ab initio molecular dynamics calculations. It was observed that the incorporation of Ag into the system decreases the root mean square displacement of the other cations and anions, reducing the scattering of phonons and thereby increasing the lattice thermal conductivity. Moreover, the calculations on the formation energy have revealed the reason for the structural transformation of CTS and similar diamond-like structures toward high symmetry polymorphs by external doping. The increase in zT is directly related to the optimization of the band gap and the weighted mobility, which have been investigated experimentally and using the first principle method.

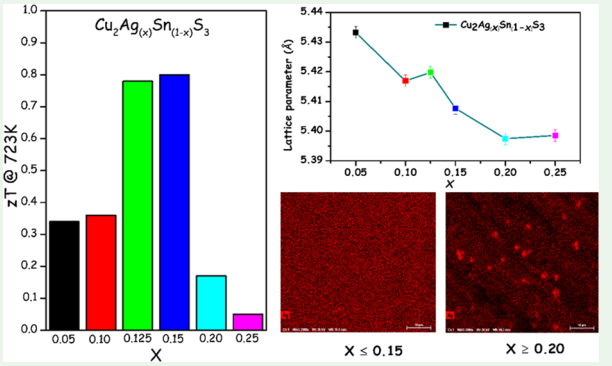

KEYWORDS: *Cu_2SnS_3, copper tin sulfide, CTS, thermoelectricity, chalcogenides, mechanical alloying, spark plasma sintering, lattice thermal conductivity, weighted mobility, DFT, AIMD*

INTRODUCTION

Heat is a low-grade energy form and a common byproduct in almost all power generation and transmission processes. Thermoelectric (TE) devices are solid-state, scalable, and noise-free, and they can convert waste heat into electrical energy. TE devices consist of several pairs of p- and n-type semiconducting legs connected electrically in series and thermally in parallel. Heat-to-electrical energy conversion of such a device is assessed by Carnot efficiency (η).[1]

$$\eta = \left(\frac{T_{hot} - T_{cold}}{T_{hot}}\right)\left[\frac{\sqrt{(1 + zT_{avg})} - 1}{\sqrt{(1 + zT_{avg})} + \left(\frac{T_{cold}}{T_{hot}}\right)}\right] \quad (1)$$

$$zT = \left(\frac{S^2}{\rho\kappa}\right)T \quad (2)$$

where T_{hot}, T_{cold}, and zT_{avg} are the hot-side temperature, cold-side temperature, and average TE figure of merit, respectively. The latter is characteristic of a given material, as defined in eq 2, where S, ρ, κ, and T are the Seebeck coefficient, electrical resistivity, thermal conductivity, and absolute temperature, respectively. Thus, p- and n-type materials presenting a high figure of merit are essential to produce high-performing TE devices. However, various physical properties that determine the zT of materials show strong interdependence, limiting its enhancement. Several strategies to enhance the zT of materials are discussed in the literature, such as nanostructuring,[2] alloying,[3] band engineering,[4] energy-filtering,[5] etc.

Cu_2SnS_3 (CTS) is a nontoxic, eco-friendly, and low-cost thermoelectric material. Although the first lab synthesized and naturally discovered CTS had a triclinic ($P1$) structure,[6] authors have diffusely reported monoclinic (Cc) CTS synthesized by high-temperature solid-state reactions from a

Received: February 15, 2023
Accepted: March 9, 2023
Published: March 22, 2023

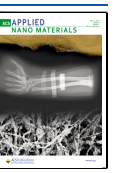

thermoelectric perspective. Frequently, a blend of cubic ($F\bar{4}3m$) and tetragonal ($I\bar{4}2m$) CTS polymorphs can be observed with monoclinic CTS. The monoclinic CTS polymorph shows low zT ∼ 0.05 above 700 K, due to its low carrier concentration and high thermal conductivity. The external cation doping at the Sn site transforms the monoclinic polymorph into cubic ($F\bar{4}3m$). It is worth mentioning that partially (SG: $I\bar{4}2m$) or fully (SG: $F\bar{4}3m$) disordered CTS polymorphs can also be obtained by synthesis methods, e.g., colloidal method[7] and high-energy reactive ball milling.[3,8] Recently, Koskela et al.[9] reported an orthorhombic ($Cmc2_1$) CTS polymorph. Polymorphism in these materials offers multiple possibilities of structural manipulation and band engineering to boost the TE performance. Moreover, Cu−Sn−S-based systems have low formation energy; therefore, they are suitable for large-scale and low-cost production. These systems are safe to use in the medium temperature range due to the high melting temperature (∼1000 K). Recent work on CTS and similar chalcogenides-based in-plane thermoelectric generators (TEGs) shows promising power output per unit active planar area.[10]

Generally, crystalline materials arrange their atoms regularly and periodically in three dimensions, according to a characteristic long-range order. Various crystalline materials also present complex crystallographic structures, also known as disordered materials, where long-range order is absent. The disordered materials are mainly characterized by structural disorder induced by the partial occupancy of cations in the unit cell and/or local deviation from the periodic arrangement. These materials can be utilized to achieve so-called phonon−glass−electron−crystal (PGEC) behavior. Disordered polymorphs of Cu_2SnS_3,[11] Cu_2SnSe_3,[12] $CuFeS_2$,[13] $Cu_5Sn_2S_7$,[14] $Cu_7Sn_3S_{10}$,[15] Cu_2ZnSnS_4 (CZTS),[16−18] and numerous other materials show remarkably suppressed thermal conductivity when compared with the corresponding ordered polymorphs. It has been verified by experimental and ab initio methods that the above-discussed cubic materials also present higher Grüneisen parameters, which is a measure of anharmonicity, in comparison with the ordered phases.[11] Lattice distortions, irregular bond length, and soft bonds cause higher anharmonicity, originating from structural disorder. Moreover, the low electronegativity difference and high covalent character of CTS bonds and band tailing enhance the electronic transport properties.[11]

Ag is the most conductive metal. Ag doping has been used to enhance (SnSe,[19] Cu_2SnZnS_4,[20] Cu_2SnSe_3,[12] etc.) and reduce (Cu_2Se,[21] Cu_2Te,[21] SnTe,[22] etc.) the carrier concentration, depending on whether the materials have high or low carrier density. In 1970, Ag-containing Cu_2Se-based materials were considered a potential candidate for radioisotope TEG.[23] At room temperature (RT), Ag-doped Cu_2Se shows multiple phases. When sintered above 410 K, it transforms its crystallographic structure into the cubic phase.[23]

Sharma et al.[20] studied the TE properties of Ag nanoparticles blended in Cu_2ZnSnS_4 (CZTS) microspheres via the microwave method followed by hot pressing. They observed that Ag nanoparticles were mainly a secondary phase in the materials, acting as a bridge between CZTS grains for electrical transport and as scattering centers for phonons. Overall, Ag-mixed CZTS presents a maximum zT of 0.14 at 623 K. Cheng et al.[24] investigated Ag substitution at the Cu site in a similar Cu_2SnSe_3 system, which resulted in a zT of ∼1 at 800 K. They extended the study by simultaneous In-doping at the Sn site and introduction of Ag_2S, forming a $Cu_{1.85}Ag_{0.15}Sn_{0.91}In_{0.09}Se_3$/4% Ag_2S composite. The combined effect of band structure engineering (via doping) and microstructural engineering (via Ag_2S) enhanced its zT to 1.58 at 800 K, which is 2-fold higher than Cu_2SnSe_3. In addition, Mehmood et al.[25] reported a zT of ∼0.25 for $Cu_2ZnSnSe_4$ by Ag alloying.

The present work combines a two-step high-density thermoelectric sample preparation method (high-energy reactive ball milling followed by spark plasma sintering (SPS))[26] with Ag substitution at the Sn site in CTS. Various $Cu_2Ag_{(x)}Sn_{(1-x)}S_3$ ($0.05 \leq x \leq 0.25$) samples were prepared, and their TE properties were systematically investigated. It is well known that the holes in CTS and similar systems (Cu_2SnZnS_4,[27] $Cu_2SnZnSe_4$,[28] Cu_2SnSe_3,[29] etc.) are produced by the unfilled Cu 3d orbital. The maximum contribution to the density of states (DOS) in the valence band (VB) comes from the Cu 3d orbital, followed by the S/Se 3p/4p orbital, while the contribution of the Sn 5s orbital is minimal. The Sn atoms contribute minimally to electronic transport. Thus, an effort has been made to improve the thermoelectric properties of CTS by means of Ag substitution at the Sn lattice site.

EXPERIMENTAL METHODS

$Cu_2Ag_{(x)}Sn_{(1-x)}S_3$ (x = 0.05, 0.10, 0.125, 0.15, 0.20, and 0.25) powder samples were synthesized from elemental powders using high-energy ball milling (Fritsch P4). Elemental powders of Cu, Ag, Sn, and S were fed in WC vials in a stoichiometric ratio and milled for 3 h, producing ∼6 g of the powder sample (rotation and spinning speeds of −1080 and 300 rpm, respectively). The whole synthesis process was performed in a highly controlled Ar environment (O_2 and H_2O < 10 ppm).

The as-milled powder was sintered at 400 °C for 10−15 min under 50 MPa pressure using SPS equipped with a WC die. A boron nitrate layer was applied while performing the sintering to avoid current passing through the sample and contamination from the die. The resulting samples had a density of ∼4.18 g/cm^3, which is >90% of the theoretical density for CTS.

Structural, microstructural, and chemical information on the samples was collected by combining results from X-ray diffraction (XRD), scanning electron microscopy (SEM), and energy-dispersive X-ray (EDX) spectroscopy analysis. The XRD patterns were collected in Bragg−Brentano geometry using a Bruker D8 diffractometer equipped with a Co Kα (λ = 1.7889 Å) source. SEM-EDX measurements were performed using a Jeol IT300 scanning electron microscope. Rietveld refinement[30,31] was performed on XRD data using whole powder pattern modelling (WPPM) modeling[32,33] as implemented in TOPAS 6[34] software.

Thermoelectric properties were investigated by temperature-dependent (323−723 K) resistivity (ρ), Seebeck coefficient (S), and thermal diffusivity (D) measurements. Linseis Messgeraete GmbH's LSR-3 was used for the Seebeck coefficient and resistivity measurements, whereas LFA-500 was used to measure the thermal diffusivity.

The C_p measurements were performed at 50 °C using a thermal analysis Q100 DSC instrument. The same instrument was used for heat flux measurements in a temperature span of 50−350 °C in both heating and cooling cycles. Archimedes' principle was employed for the density measurement.

A UV−vis−near-infrared (NIR) spectrophotometer with a 150 mm integrating sphere (PerkinElmer spectrophotometer, LAMBDA 750) was used to record the optical absorption spectra on several CTS samples. The absorption spectra were collected on ground samples weighing 0.10 g, which were sonicated for 4 h in 40 mL of ethanol solution.

https://doi.org/10.1021/acsanm.3c00716
ACS Appl. Nano Mater. 2023, 6, 6323−6333

COMPUTATIONAL METHODS

The first-principles calculations were conducted using the Vienna Ab initio Simulation Package (VASP).[35,36] The Perdew–Burke–Ernzerhof (PBE)[37] under the generalized gradient approximation (GGA) was used for the self-consistent field (SCF) calculations. The electron–ion interaction was described using the projector augmented wave (PAW) method with the VASP recommended potentials.

The calculations were performed on a 72-atom supercell containing 24-Cu, 12-Sn, and 36-S atoms (CTS). Three other supercells were also modeled with single, double, and triple Sn atoms replaced by Ag atoms and represented as CTS (Cu_2SnS_3), CTS-1 ($Cu_2Ag_{0.083}Sn_{0.91}S_3$), CTS-2 ($Cu_2Ag_{0.16}Sn_{0.84}S_3$), and CTS-3 ($Cu_2Ag_{0.25}Sn_{0.75}S_3$), respectively.

The wave function obtained with the SCF calculations was then used to perform the density of states (DOS) calculations with a Heyd–Scuseria–Ernzerhof (HSE06)[38] potential. The cutoff energy for the plane wave basis set was set to 400 eV, and the electronic convergence was set to 10^{-6} eV for DOS calculations. Brillouin zone sampling was performed on a k-mesh of 4 × 4 × 4 centered at the Γ-point. Furthermore, the calculations of the formation energy were performed on the supercells described above.

Ab initio molecular dynamics (AIMD) calculations were performed to investigate the temperature-dependent time evolution of the different Ag-doped CTS systems. The electron-exchange–correlation function was approximated by the PBE. Again, all calculations were performed with an energy cutoff of 400 eV and a Gaussian charge smearing of 0.1 eV. The irreducible Brillouin zone was sampled on a single point using a 1 × 1 × 1 Monkhorst–Pack γ-centered k-grid. A canonical (NVT) ensemble with a Nose–Hoover thermostat was used for AIMD calculations. In each case, the system was allowed to evolve over 10 000 steps with a time step of 2 fs, corresponding to a total simulation time of 20 ps. The AIMD simulations were performed at 450, 500, and 550 K. From the calculated trajectories of the AIMD simulations, the vibrational density of states (VDOS) was calculated by computing the Fourier transform of the velocity autocorrelation function. The VDOS was also calculated with density functional perturbation theory (DFPT) using the Phonopy code.[39] For DFPT calculations, the electronic convergence was set to 10^{-8} eV. The VDOS was calculated by sampling the Brillouin zone on a grid of 20 × 20 × 20 q-mesh.

RESULTS AND DISCUSSION

XRD data collected on all of the $Cu_2Ag_{(x)}Sn_{(1-x)}S_3$ (x = 0.05, 0.10, 0.125, 0.15, 0.20, and 0.25) samples are shown in Figure 1. Samples with different weight percentages of Ag showed a cubic Sphalerite-like ($F\bar{4}3m$) phase, characterized by (111), (200), (220), and (311) Bragg peaks at $2\theta \sim$ 33.5, 38.7, 55.8, and 66.9°, respectively. We do not observe additional Bragg peaks for Ag in XRD patterns, implying that Ag substitution with different weight fractions was successful, and $Cu_2Ag_{(x)}Sn_{(1-x)}S_3$ samples belong to the disordered cubic phase (lattice parameter shown in Figure 2b). Moreover, with the increased amount of Ag substitution, Bragg peaks show a shift toward higher 2θ or decreased interplanar spacing (see the inset of Figure 1).

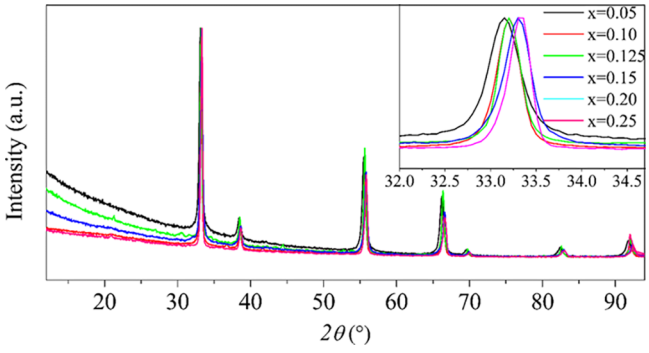

Figure 1. XRD data on $Cu_2Ag_{(x)}Sn_{(1-x)}S_3$ samples. The inset shows the highest intensity Bragg peak shift with increased Ag substitution.

The information on structure, lattice parameters, strain, and domain size was extracted using Rietveld refinement (shown in Figures 2a and S1). Due to the smaller atomic radius of Ag than that of Sn, the shrinking of lattice parameters with increased Ag substitution can be observed (shown in Figure 2b). The lattice parameter decreases up to $Cu_2Ag_{(x)}Sn_{(1-x)}S_3$ (x = 0.20) and then saturates, possibly reaching the solubility limit of Ag in the CTS lattice. The average domain size of the samples is ∼50 nm, and no significant microstrain was observed in the samples. Literature reports that the CTS samples prepared via the widely used solid-state reaction show significant grain growth, where the average crystallite size ranges from a few hundreds of nanometers to several microns.[40]

SEM micrographs and SEM-EDX analysis on sample surfaces showed dense microstructures with almost no porosity. The grains of the samples are much smaller than the magnification of the microscope (shown in Figure S2). Chemical maps were collected, and Cu, Sn, and S showed a homogeneous chemical distribution for most samples. However, samples with $x \geq 0.20$ showed a nonhomogeneous chemical distribution of Ag (shown in Figures 3 and S3). Furthermore, Rietveld refinement revealed that the lattice parameters also do not decrease for x = 0.20 and 0.25 samples, implying the excess of Ag precipitates as a metallic phase in the doped matrix. A similar observation was made by Sharma et al.[20] for Cu_2SnZnS_4 on adding Ag nanoparticles.

Temperature-dependent thermoelectric measurements on $Cu_2Ag_{(x)}Sn_{(1-x)}S_3$ ($0.05 \leq x \leq 0.25$) samples are shown in Figure 4. All of the CTS samples show p-type, degenerate semiconductor-like behavior, confirmed by the positive value of the Seebeck coefficient and increasing resistivity in temperature. With the increased Ag substitution, samples show decreasing absolute Seebeck coefficients due to increased carrier concentration. Even with the lowest Ag (x = 0.05) substitution, CTS samples showed a degenerate or metal-like nature of resistivity, ranging from 170 to 180 $\mu\Omega$ m. For x = 0.05–0.15, the absolute Seebeck coefficient and resistivity also decreased with increasing Ag substitutions. Among various Ag-doped samples, x = 0.15 showed the lowest value of resistivity in the measured temperature span, i.e., 4–8 $\mu\Omega$ m, which is significantly lower than undoped disordered CTS samples (∼5000–2000 $\mu\Omega$ m).[11] Heavily doped CTS samples prepared via different synthesis routes have shown comparable values of resistivity/conductivity.[41−43] x = 0.20 and 0.25 samples show anomalous values of S and ρ, likely caused by the interplay between carrier concentration and mobility, as these samples have some Ag present in the lattice and rest in bulk.

The unreacted metallic Ag grains in bulk would introduce free electrons into the system. However, we do not observe any sharp decrease in S and a simultaneous increase in ρ at elevated temperatures, an effect of bipolar conduction. In such cases, the thermopower (S) is a weighted average of Seebeck coefficients associated with both types of carriers. Opposite signs of both charge carriers diminish the thermopower of the material. The x = 0.25 and 0.20 samples, respectively, show S ∼ 20–40 and 30–60 μV/K in the temperature range of 300–

https://doi.org/10.1021/acsanm.3c00716
ACS Appl. Nano Mater. 2023, 6, 6323–6333

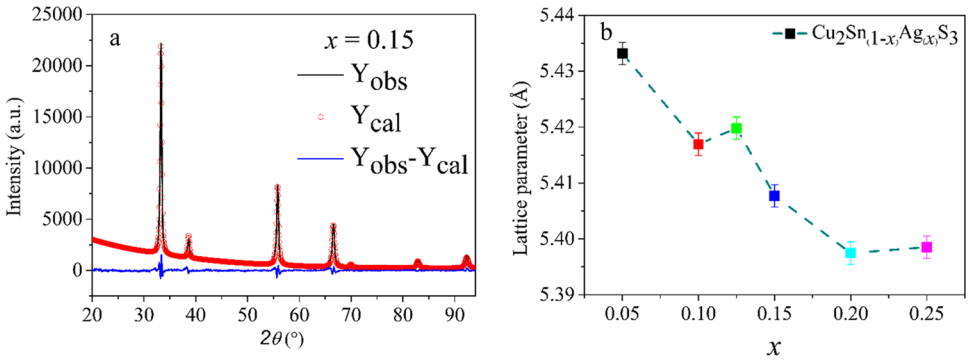

Figure 2. (a) Rietveld refinement performed on the x = 0.15 sample, (b) change in lattice parameters with increased Ag substitution. (Rietveld refinement data on all of the samples are shown in Figure S1 and Tables S1−S3).

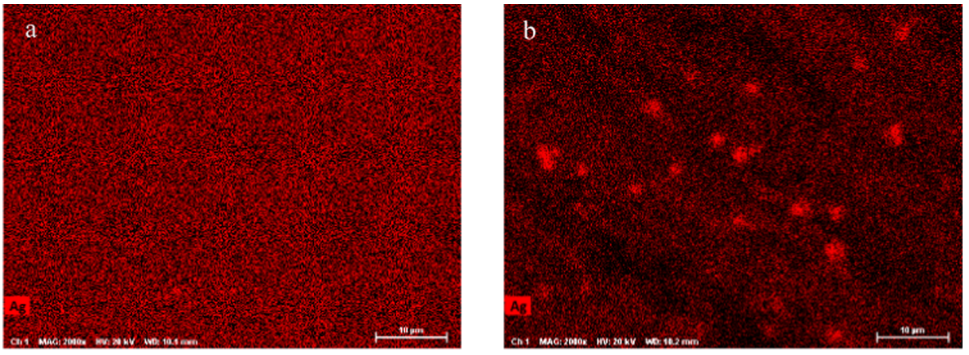

Figure 3. Chemical maps collected using SEM-EDX on $Cu_2Ag_{(x)}Sn_{(1-x)}S_3$ samples. Showing a homogeneous and nonhomogeneous Ag substitution on (a) $x \leq 0.15$ and (b) $x \geq 0.20$ samples, respectively. (Elemental maps on all elements are shown in Figure S3).

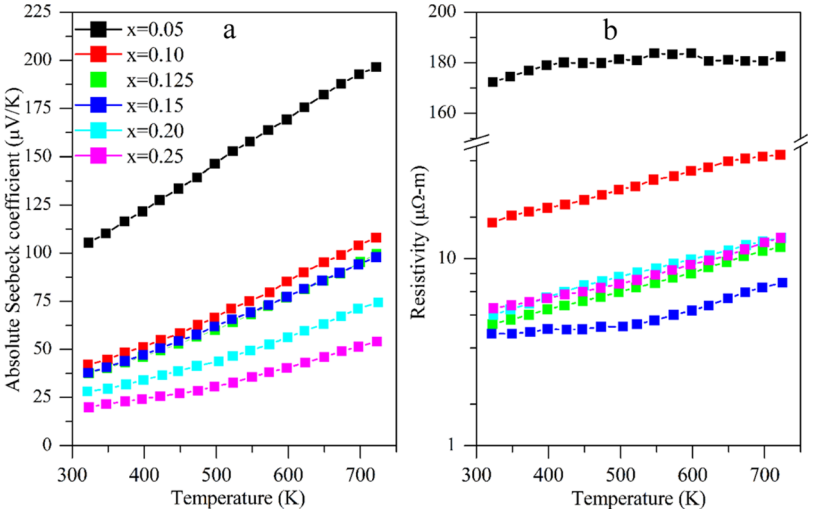

Figure 4. (a) Temperature-dependent absolute Seebeck coefficient (S) and (b) resistivity (ρ) measurements on $Cu_2Ag_{(x)}Sn_{(1-x)}S_3$ ($0.05 \leq x \leq 0.25$) samples.

723 K, which is 1 order of magnitude lower than undoped CTS[44] prepared by various synthesis and sintering techniques. It is worth mentioning here that with a small amount of external doping, x = 0.05, S was 100−200 μV/K in the same temperature span, which is comparable to the literature.[45]

In a recent work, Snyder et al.[46] proposed the calculation of the weighted mobility (μ_W) from the experimentally measured Seebeck coefficient and resistivity, under the assumption that the charge transport is dominated by a single band. In this context, we calculated the weighted mobility of $Cu_2Ag_{(x)}Sn_{(1-x)}S_3$ ($0.05 \leq x \leq 0.25$) samples (see Figure 5).

For the calculation of μ_W, the following formula from the aforementioned work is used

$$\mu_W = \left(\frac{331}{\rho}\right)\left(\frac{T}{300}\right)^{-3/2}\left[\frac{\exp\left(\frac{|S|}{86.3} - 2\right)}{1 + \exp\left(-\frac{|S|}{17.3} + 5\right)} + \frac{\frac{3}{\pi^2}\frac{|S|}{86.3}}{1 + \exp\left(\frac{|S|}{17.3} - 5\right)}\right] \quad (3)$$

https://doi.org/10.1021/acsanm.3c00716
ACS Appl. Nano Mater. 2023, 6, 6323−6333

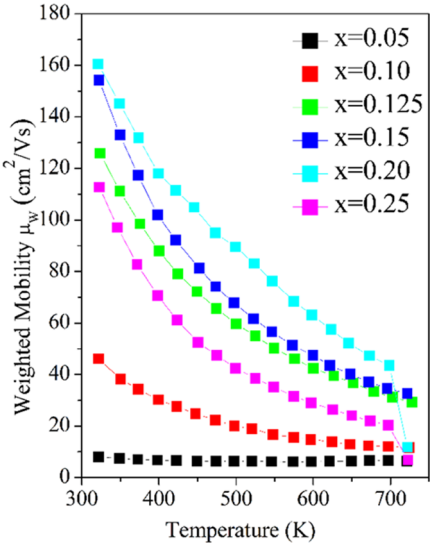

Figure 5. Variation of weighted mobility (μ_W) with temperature for various $Cu_2Ag_{(x)}Sn_{(1-x)}S_3$ ($0.05 \leq x \leq 0.25$) samples.

Here, μ_W, ρ, S, and T are expressed in the units of $cm^2/(V\ s)$, mΩ cm, μV/K, and K, respectively.

Due to the inherent $T^{-3/2}$ term in the weighted mobility formula, a decreasing trend with temperature was observed, indicating the acoustic phonon scattering of charge carriers. The transport properties (S and ρ) show an optimization with increasing Ag content in the samples. The weighted mobility of samples has an increasing trend with Ag substitution ($x \leq 0.20$), contrary to the general view of Hall mobility, which decreases with carrier concentration. However, the heavily doped CTS sample $x = 0.25$ showed a drop in weighted mobility. This is in agreement with the XRD and SEM chemical maps showing the threshold ($x \leq 0.20$) of Ag substitution in the CTS lattice. The corresponding effects can also be observed in the transport properties of heavily doped CTS samples ($x = 0.20$ and 0.25). The sample with the highest Ag precipitate in bulk ($x = 0.25$) shows an intermediate value of weighted mobility, suggesting that Ag excess in bulk acts as scattering centers for charge carriers, decreases the weighted mobility, and, in turn, increases the resistivity of the sample (see Figure 4b).

The electronic DOS was calculated to validate the experimentally observed results. The experimental results showed that the increased Ag content in the prepared samples leads to a decrease in both S and ρ values. This can be explained by considering that Cu, Sn, and S's oxidation states in CTS are +1, +4, and −2, respectively. Therefore, the nonisoelectronic replacement of Sn by an Ag atom would lead to additional holes in the system, enhancing the valence band edge, see Figure 6.

The DOS of CTS and Ag-substituted CTS systems is higher at the valence side than the conduction, confirming the p-type nature of all calculated supercells. The valence band edge shifted toward higher energy with the increased Ag content. The Fermi level lies deep inside the VB for Ag-substituted systems, with a shift of the Fermi level inside the valence band increasing with the substitution. Thus, the increased substitution of Ag in the lattice would enable a more degenerate semiconductor-like nature in CTS and other similar systems, such as Cu_2SnZnS_4,[20] $CuFeS_2$,[47] Cu_2SnSe_3,[48] etc.

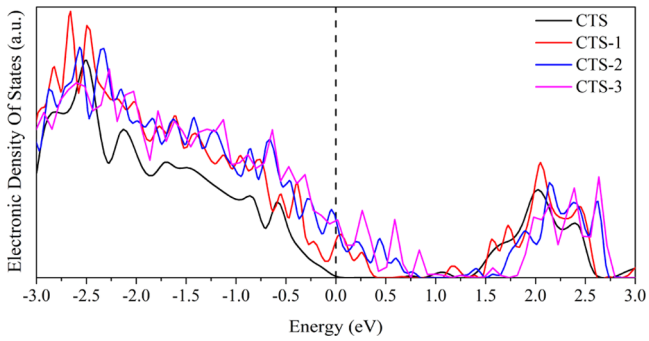

Figure 6. Calculated DOS on monoclinic CTS, and 1 Ag, 2 Ag, and 3 Ag atom-substituted CTS systems, shown as CTS (Cu_2SnS_3), CTS-1 ($Cu_2Ag_{0.083}Sn_{0.91}S_3$), CTS-2 ($Cu_2Ag_{0.16}Sn_{0.84}S_3$), and CTS-3 ($Cu_2Ag_{0.25}Sn_{0.75}S_3$), respectively. Here, the dotted line represents the Fermi level, set at zero. The atomic projected DOS for all calculated structures is shown in Figure S4.

The optical absorption spectra were collected on $Cu_2Ag_{(x)}Sn_{(1-x)}S_3$ (x = 0.05, 0.10, 0.125, 0.15, 0.20, and 0.25) samples (shown in Figure S5). Figure 7 shows the

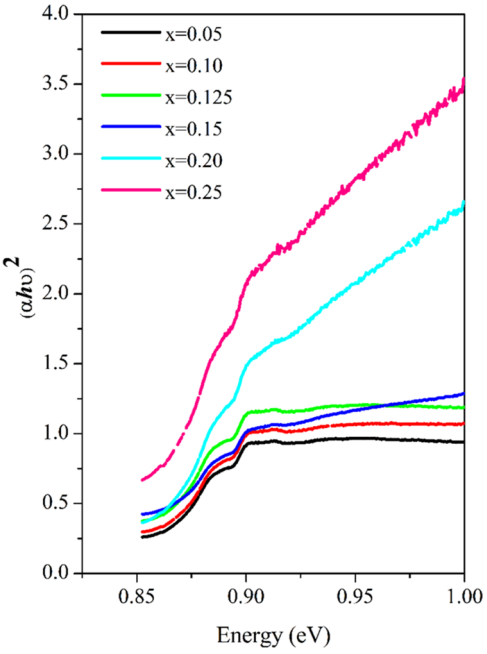

Figure 7. Band gap measurements performed on various $Cu_2Ag_{(x)}Sn_{(1-x)}S_3$ ($0.05 \leq x \leq 0.25$) samples.

estimated band gap (E_g) by linear extrapolation in the Tauc plot, using the equation $\alpha h\nu = A(h\nu - E_g)^{1/2}$, where α, h, ν, A, and E_g are the absorption coefficient, Planck constant, frequency, transmission constant, and band gap, respectively. These measurements are qualitatively in agreement with the calculated DOS, confirming that by increasing Ag substitution, the band gap decreases. The band gap values for undoped ordered and disordered CTS polymorphs are ∼0.99 and ∼0.95 eV, respectively.[11] In the present work, the $x = 0.05$ sample showed a lower band gap of ∼0.85 eV, which further decreased with increased Ag substitution (shown in Figure 7).

An essential aspect of external doping in the CTS system is the structural transformation from an ordered monoclinic to a disordered cubic phase, which means a tendency toward higher symmetry. To understand this, additional DFT calculations

https://doi.org/10.1021/acsanm.3c00716
ACS Appl. Nano Mater. 2023, 6, 6323−6333

were performed to calculate the formation energy of the three doped systems concerning the monoclinic system. Table 1

Table 1. Formation Energy per Unit Atom of CTS and Ag-Doped CTS Systems

system	configuration	energy of the system (eV)	formation energy per unit atom (eV/atom)
CTS	Cu-24, Sn-12, S-36	−308.037	−24.117
CTS-1	Cu-24, Ag-1, Sn-11, S-36	−305.925	−23.135
CTS-2	Cu-24, Ag-2, Sn-10, S-36	−303.680	−22.020
CTS-3	Cu-24, Ag-3, Sn-9, S-36	−301.438	−20.908

reports the formation energy calculated for the four systems. Formation energy calculations confirm that the monoclinic CTS structure is the most stable, with the lowest formation energy. The introduction of Ag at the Sn site increases the formation energy, making the Ag-doped systems less stable in the monoclinic form. Therefore, external doping drives the system toward higher symmetry structures in CTS and various similar diamond-like materials.[11,40,42,49−51]

The power factor (PF ∼ 12.8 μW/(K^2 cm)) for the x = 0.15 sample is high compared to the literature for a similar system. It should be noted that it is ∼10- and ∼3-fold higher than, respectively, undoped disordered CTS[3] and CTS with the smallest domain size, i.e., 12 nm.[26] Similar Cu_3SnS_4,[52] $Cu_5Sn_2S_7$,[53] and $Cu_7Sn_3S_{10}$[15] systems also show comparable values of PF at the same temperature range. The highest PF of the x = 0.15 sample is followed by x = 0.125 and 0.20, with PF values of ∼8 and ∼4 μW/(K^2 cm), respectively. The x = 0.10 sample showed an intermediate PF of ∼3.0 at 723 K, while x = 0.25 and 0.05 samples presented the lowest PF of ∼1.75 μW/(K^2 cm) at the same temperature.

The highest PF of the x = 0.15 sample is supported by its moderate Seebeck coefficient and very low electrical resistivity, and its resistivity is lowest among all $Cu_2Ag_{(x)}Sn_{(1-x)}S_3$ (x = 0.05, 0.10, 0.125, 0.15, 0.20, and 0.25) samples. Although the x = 0.25 sample also has lower electrical resistivity, the extremely suppressed Seebeck coefficient diminishes its power factor, making it the same as the lowest doped x = 0.05 sample, see Figure 8.

The total thermal conductivity was calculated as $\kappa = DC_pd$, where D, C_p, and d are the diffusivity, specific heat capacity, and density, respectively. At 323 K, the C_p values for $Cu_2Ag_{(x)}Sn_{(1-x)}S_3$, ($0.05 \le x \le 0.25$) samples were in the range of 0.369−0.394 J/(g K) (values for all of the samples are reported in Table S4). The C_p for Ag-substituted samples is lower than the reported value for undoped CTS (∼0.44 J/(g K)).[49] This reduction is due to the substitution of heavier (Sn) atoms with comparatively lighter (Ag) atoms. Additionally, heat flux measurements in two successive heating and cooling cycles in the temperature span of 325−625 K showed that the samples are thermally stable (see Figure S6).

Ag substitution significantly reduced the electrical resistivity of CTS, resulting in a higher PF. Nevertheless, increased charge carrier density also increases the thermal conductivity of the samples. The total thermal conductivity of $Cu_2Ag_{(x)}Sn_{(1-x)}S_3$ (x = 0.05, 0.10, 0.125, 0.15, 0.20, and 0.25) samples grows with increasing Ag substitution (Figure 9). The decreasing trend of κ with temperature shows

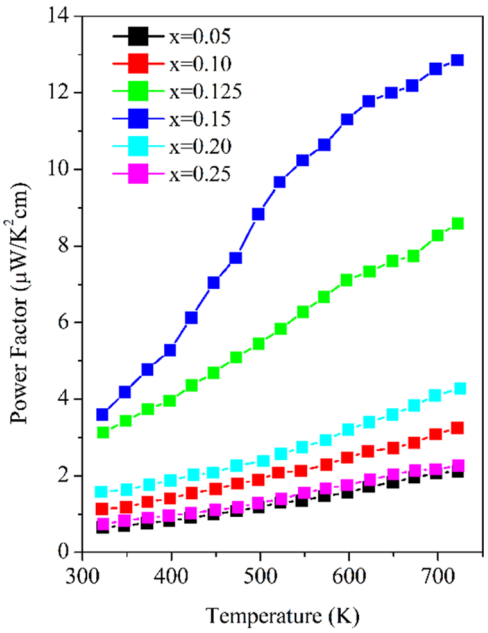

Figure 8. Temperature-dependent power factor (PF) calculated as PF = S^2/ρ for $Cu_2Ag_{(x)}Sn_{(1-x)}S_3$ ($0.05 \le x \le 0.25$) samples.

increased phonon−phonon or Umklapp scattering. However, the thermal conductivity appears to be governed by a complex mechanism. The x = 0.05 sample showed the lowest κ of ∼0.5 W/(m K), and the x = 0.10 and 0.125 samples showed a similar κ of ∼0.8 at 723 K. The sample with the highest PF (x = 0.15) showed a further increase in κ of ∼1.2 W/(m K) at the same temperature. The x = 0.25 sample showed the highest κ of ∼6−3 W/(m K), which is ∼6-fold higher than the lowest Ag-doped (x = 0.05) sample.

Total thermal conductivity (κ) consists of lattice (κ_l) electronic (κ_e) contributions. The lattice component of thermal conductivity ($\kappa_l = \kappa - \kappa_e$) is estimated via the Wiedemann Franz law ($\kappa_e = L_o\sigma T$), where L_o is the Lorenz number. The Lorenz number is calculated via a widely accepted method of fitting the Seebeck coefficient data to the reduced chemical potential. Besides, $L_o = 1.5 + \exp\left[-\frac{|S|}{116}\right]$ (where L_o is in 10^{-8} W Ω/K^2 and S in μV/K)[54] has been proposed as a good approximation for single parabolic band scattering (shown in Figure S7a). However, for materials with complex and multiple scattering mechanisms, this estimation could introduce large errors.

Samples with x = 0.125 and 0.15 have shown a complex optimization of S and ρ, resulting in a high PF. The κ_l computed via the Wiedemann Franz law for these two samples showed negative values above 425 K. Ballikaya et al.[21] also observed difficulty in the determination of lattice thermal conductivity in Ag-doped systems. These systems were highly conductive due to the contribution of charge carriers (holes) and mobile ions (Ag^+) in the conduction, and it is not clear which form of the Wiedemann Franz law should be applied to determine κ_l. However, samples x = 0.05, 0.10, 0.20, and 0.25 show positive and increasing κ_l with increased Ag substitution. It is important to note that Figure 9b only depicts the trend of lattice thermal conductivity with Ag substitution, not its absolute value.

The electronic contribution to the thermal conductivity is shown in Figure S7b. The trend of κ_e with Ag doping is similar

https://doi.org/10.1021/acsanm.3c00716
ACS Appl. Nano Mater. 2023, 6, 6323−6333

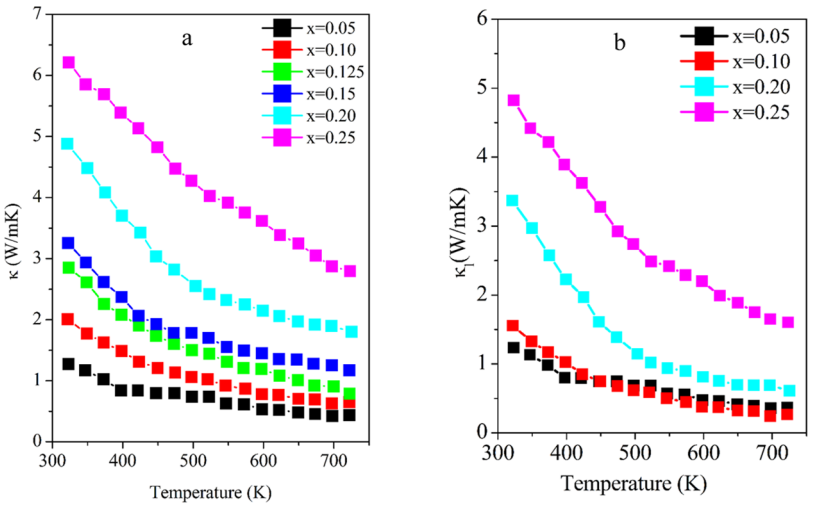

Figure 9. (a) Total thermal conductivity (κ) and (b) lattice thermal conductivity (κ_l) for $Cu_2Ag_{(x)}Sn_{(1-x)}S_3$ ($0.05 \leq x \leq 0.25$).

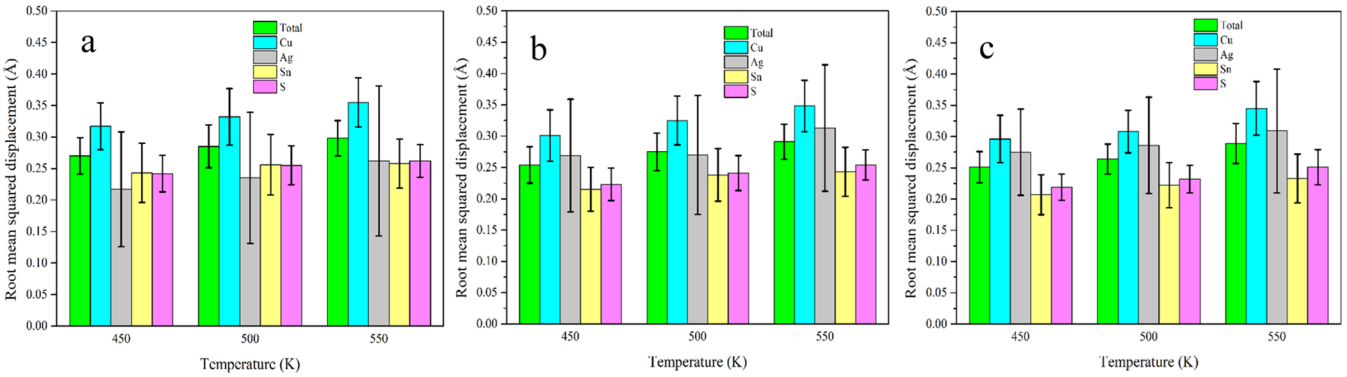

Figure 10. Temperature-dependent root mean square displacement (RMSD) for (a) 1 Ag, (b) 2 Ag, and (c) 3 Ag atom-substituted CTS systems.

to that of electrical resistivity, owing to the linear relationship with conductivity. The κ_e values are not sufficiently high to explain the significant increase in total thermal conductivity. An interesting effect of Ag doping in the CTS system was the improvement of lattice thermal conductivity (κ_l), see Figure 9b. When external dopants are introduced into the system, they generally act as scattering centers for phonons that reduce the lattice thermal conductivity. The effect of Ag doping in the system to improve TE performance has resulted in an atypical behavior of lattice thermal conductivity.

To gain insights into the atypical behavior, the temperature-dependent time evolution of the Ag-doped systems was investigated. From the AIMD trajectories, the root mean square displacement (RMSD) was calculated for different cations and anions, see Figure 10. The RMSD values with errors are given in Table S5. A relatively large RMSD value generally means that the corresponding atom vibrates with a higher amplitude about its equilibrium position, due to the weak restoring forces on the vibrating atoms or soft bonds. The increase in Ag concentration resulted in a decrease in the RMSD of all cations and anions, except Ag. The increase in temperature leads to an increase in the RMSD value for all atoms, a typical temperature-dependent behavior. From the results, it appears that the introduction of Ag into the system suppresses the RMSD of other atoms and reduces the overall RMSD, see Figure S8. The reduced RMSD of the cations/anions indicates a stronger interaction between the atoms, which reduces the scattering of the phonons and thus increases the κ_l with Ag substitution. Similar results were obtained by Liu et al.[55] where the Ag doping induced abnormal lattice thermal conductivity in Cu_2Se with an increasing Ag concentration. Moreover, Cao et al.[56] also observed an increase in lattice thermal conductivity in CTS via Fe^{3+} doping.

To further support the argument, we looked at the VDOS calculated using two different methods, one using the DFPT and the other using the AIMD trajectories, as shown in Figure 11a,c, respectively. Although the two methods used to calculate the VDOS were different, the results were consistent. We observed that with the introduction of Ag into the system, the magnitude of VDOS at low frequencies decreased (<3 THz), and a small shift toward higher frequencies was observed, see magnified VDOS in Figure 11b,d. This would reduce the scattering of low-frequency phonons, which are primarily responsible for thermal transport. Apart from this, the VDOS calculated from the AIMD trajectories also showed broadening, as it was calculated at a higher temperature, i.e., 450 K.

Overall, x = 0.15 and 0.125 samples show the highest zT of ~0.8 at 723 K, see Figure 12a. Although x = 0.125 has a slightly lower PF of 8 $\mu W/(K^2\ cm)$ than the x = 0.15 (PF ~ 12.8 $\mu W/(K^2\ cm)$) sample, the lower thermal conductivity of the x = 0.125 sample increases its zT. The highest zT of x = 0.15 and 0.125 samples was followed by the second highest zT of ~0.35 for the x = 0.05 and 0.10 samples. Another sample, x = 0.20, showed a zT of ~0.15 at 723 K. The sample containing the highest amount of Ag (x = 0.25) deteriorates the zT ~ 0.05, due to its high thermal conductivity and low Seebeck

https://doi.org/10.1021/acsanm.3c00716
ACS Appl. Nano Mater. 2023, 6, 6323−6333

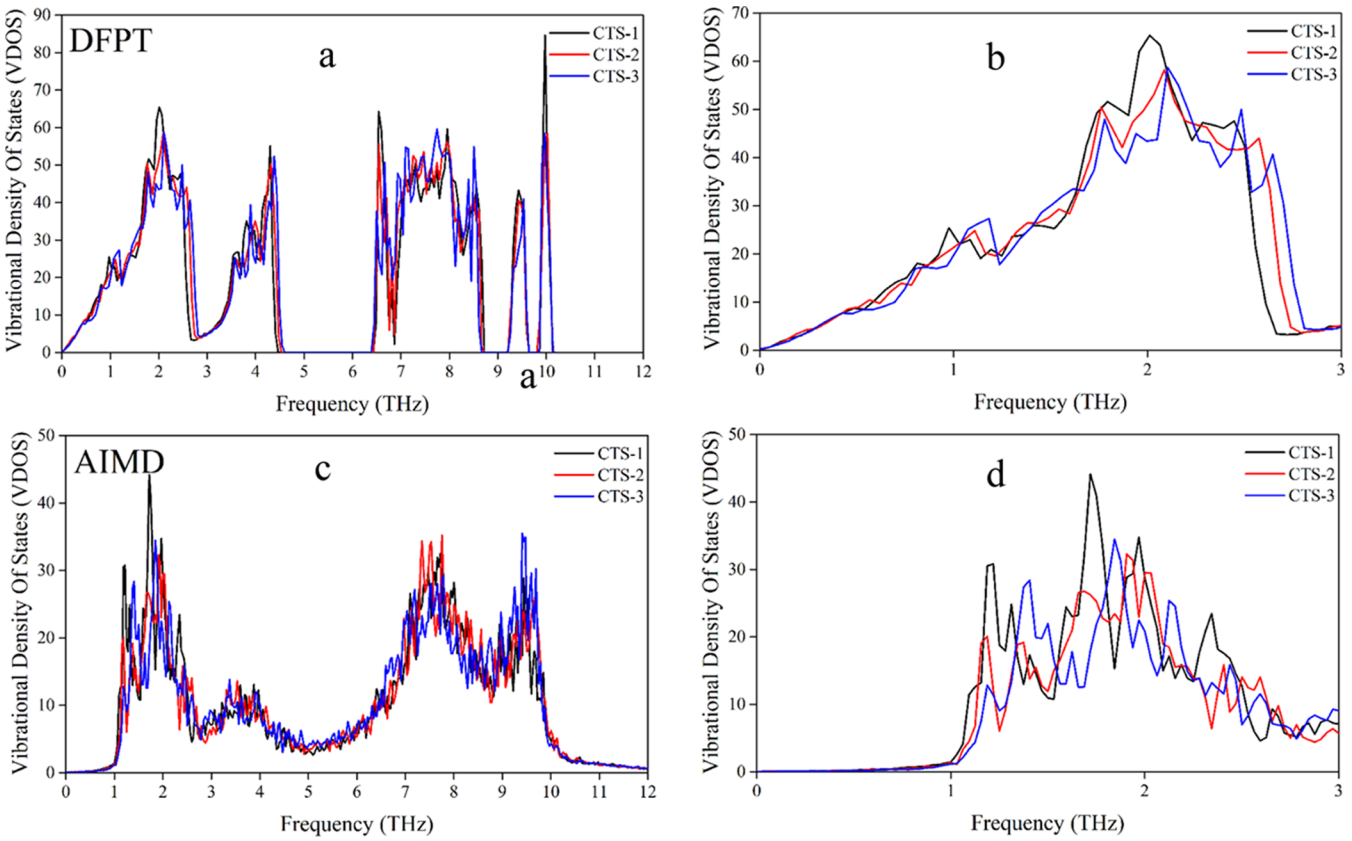

Figure 11. Vibrational density of states (VDOS) calculated via (a) DFPT and (c) AIMD (at 450 K) for 1 Ag, 2 Ag, and 3 Ag atom-substituted CTS systems. The adjacent figures (b) and (d) show the magnified VDOS at a low-frequency span via DFPT and AIMD, respectively.

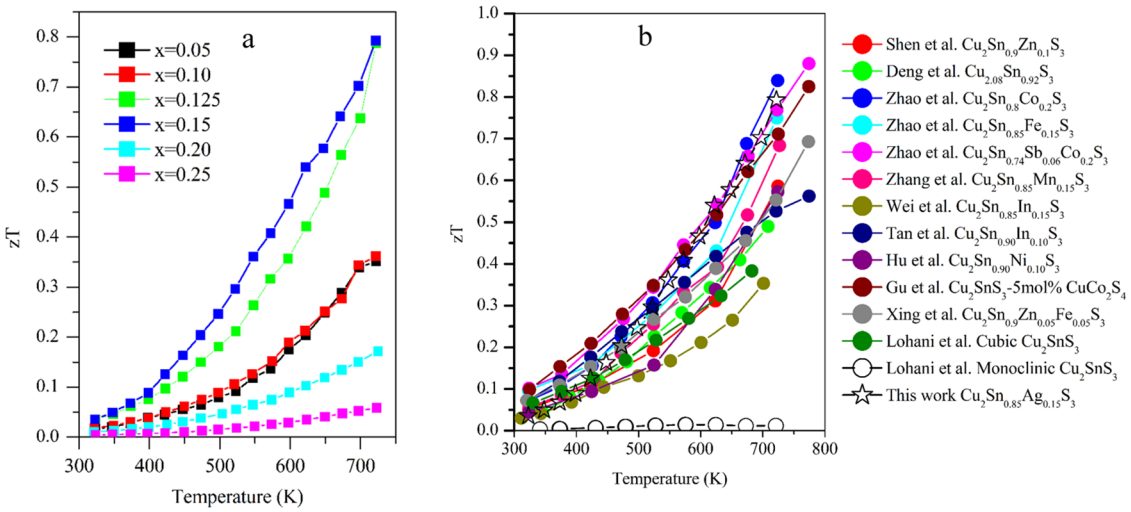

Figure 12. (a) Thermoelectric figure of merit for $Cu_2Ag_{(x)}Sn_{(1-x)}S_3$, ($0.05 \leq x \leq 0.25$) samples, and (b) a comparison between various investigations performed on CTS systems in the literature.

coefficient. Interestingly, the samples with intermediated weighted mobility and band gap (x = 0.15) show higher PF and zT, indicating an optimization of charge and heat transport.

Figure 12b shows a comparison of various investigations performed on CTS systems. Our past works showed that the pristine disordered (cubic) CTS polymorph has a higher thermoelectric figure of merit than ordered (monoclinic).[11,26] Initially, researchers tried to optimize the thermoelectric properties of CTS via various single-element doping, such as Zn,[42] Cu,[45] Co,[40] Fe,[49] Mn,[43] In,[57] and Ni.[58] Subsequently, simultaneous doping of two elements was tested in CTS, e.g., Co−Sb[59] and Zn−Fe.[60] Recently, researchers have tried to increase the thermoelectric figure of merit of CTS via twin boundary engineering,[7] dense dislocation,[61] 3D modulation doping,[62] and introduction of superparamagnetic nanoparticles.[63] However, in the present work, the $Cu_2Ag_{(x)}Sn_{(1-x)}S_3$ (x = 0.15) sample prepared via a two-step method (mechanical alloying followed by SPS) presented one of the highest zT values reported for CTS. Ag doping in CTS yields ∼16 times

https://doi.org/10.1021/acsanm.3c00716
ACS Appl. Nano Mater. 2023, 6, 6323−6333

higher zT than pristine monoclinic CTS reported in the literature. Although Co doping,[40] simultaneous Co−Sb,[59] and modulation doping via $CuCo_2S_4$[62] showed slightly higher zT than Ag-doped CTS, Ag is a nontoxic material. Additionally, the two-step method presented in this work is less time- and resource-consuming, consequently, cost-effective.

CONCLUSIONS

Herein, various Ag-substituted disordered $Cu_2Ag_{(x)}Sn_{(1-x)}S_3$ ($0.05 \leq x \leq 0.25$) polymorph samples were stabilized by a two-step synthesis method, and experimental and computational methods were employed to study their thermoelectric properties. Rietveld refinement of XRD patterns and SEM-EDX chemical maps confirmed successful Ag substitution at the Sn site up to $x \leq 0.15$. For samples $x \geq 0.20$, some Ag substituted Sn in the lattice; the rest was diffusely distributed in bulk as metallic Ag. The $Cu_2Ag_{(x)}Sn_{(1-x)}S_3$, $x = 0.15$ sample presented an ∼10-fold higher PF (∼12.8 μW/(K^2 cm)) than that reported for undoped cubic CTS (PF ∼ 1.1 μW/(K^2 cm)). However, due to the interplay between κ and PF, $x = 0.125$ and 0.15 samples showed the highest zT of ∼0.8 at 723 K. First-principles DFT simulations revealed suppression of the band gap with increased Ag substitution at the Sn site. The optical absorption spectra measurements on various $Cu_2Ag_{(x)}Sn_{(1-x)}S_3$ confirm the DFT results. The lattice thermal conductivity depicted an unconventional behavior, i.e., enhancement with Ag substitution. AIMD and DFPT were employed to shed light on the atypical behavior. It was observed that the introduction of Ag in the system was suppressing the RMSD of other atoms. Due to the reduction of RMSD, a reduction in the scattering of the phonons would occur, thus increasing the κ_l. The results were also supported by VDOS calculations using AIMD and DFPT. The two-step sample preparation method combined with doping is relatively inexpensive and sustainable, as it does not require thermal treatment at very high temperatures. A high zT of ∼0.8 was achieved by optimizing various TE parameters (S, ρ, μ_W, κ, and E_g).

ASSOCIATED CONTENT

Supporting Information

The Supporting Information is available free of charge at https://pubs.acs.org/doi/10.1021/acsanm.3c00716.

> Rietveld refinement and corresponding information; morphological images; SEM chemical maps; optical absorption spectra; atomic projected density of states (DOS) plots; specific heat capacity (C_p); heat flow measurement cycles; calculated Lorenz number (L_o) and electronic contribution to the thermal conductivity (κ_e); AIMD temperature-dependent RMSD values; and temperature-dependent total RMSD (PDF)

AUTHOR INFORMATION

Corresponding Author

Paolo Scardi − *Department of Civil, Environmental & Mechanical Engineering, University of Trento, 38123 Trento, Italy;* orcid.org/0000-0003-1097-3917; Email: paolo.scardi@unitn.it

Authors

Ketan Lohani − *Department of Civil, Environmental & Mechanical Engineering, University of Trento, 38123 Trento, Italy;* orcid.org/0000-0003-1059-6744

Himanshu Nautiyal − *Department of Civil, Environmental & Mechanical Engineering, University of Trento, 38123 Trento, Italy;* orcid.org/0000-0003-2103-4130

Narges Ataollahi − *Department of Civil, Environmental & Mechanical Engineering, University of Trento, 38123 Trento, Italy;* orcid.org/0000-0002-8135-6054

Umberto Anselmi-Tamburini − *Department of Chemistry, University of Pavia, 27100 Pavia, Italy;* orcid.org/0000-0002-8936-0170

Carlo Fanciulli − *National Research Council of Italy—Institute of Condensed Matter Chemistry and Technologies for Energy (CNR-ICMATE), 23900 Lecco, Italy*

Complete contact information is available at: https://pubs.acs.org/10.1021/acsanm.3c00716

Author Contributions

K.L. contributed to conceptualization, original draft writing, and structural and transport property measurements. H.N. performed DFT, DFPT, and AIMD simulations and contributed to the writing. N.A. performed and analyzed optical absorption measurements. U.A.-T. performed the spark plasma sintering. C.F. performed the heat flux and specific heat measurements. P.S. supervised the research and acquired the funding. All of the authors contributed to the discussion, review-writing, editing, and proofreading.

Notes

The authors declare no competing financial interest.

ACKNOWLEDGMENTS

The authors thank Dr. Mirco D'Incau for their technical help and valuable suggestions. This research takes place within the action "Research Poles", section "Research and infrastructures", in the Modeling & Simulation area of the Department of Civil, Environmental & Mechanical Engineering (DICAM), University of Trento.

REFERENCES

(1) Goldsmid, H. J. *Introduction to Thermoelectricity*, Springer Series in Materials Science; Springer: Berlin, Heidelberg, 2010; Vol. *121*, DOI: 10.1007/978-3-642-00716-3.

(2) Baláž, P.; Dutková, E.; Levinský, P.; Daneu, N.; Kubíčková, L.; Knížek, K.; Baláž, M.; Navrátil, J.; Kašparová, J.; Ksenofontov, V.; Möller, A.; Hejtmánek, J. Enhanced Thermoelectric Performance of Chalcopyrite Nanocomposite via Co-Milling of Synthetic and Natural Minerals. *Mater. Lett.* **2020**, *275*, No. 128107.

(3) Lohani, K.; Isotta, E.; Ataollahi, N.; Fanciulli, C.; Chiappini, A.; Scardi, P. Ultra-Low Thermal Conductivity and Improved Thermoelectric Performance in Disordered Nanostructured Copper Tin Sulphide (Cu_2SnS_3, CTS). *J. Alloys Compd.* **2020**, *830*, No. 154604.

(4) Wei, T.-R.; Qin, Y.; Deng, T.; Song, Q.; Jiang, B.; Liu, R.; Qiu, P.; Shi, X.; Chen, L. Copper Chalcogenide Thermoelectric Materials. *Sci. China Mater.* **2019**, *62*, 8−24.

(5) Narducci, D.; Selezneva, E.; Cerofolini, G.; Frabboni, S.; Ottaviani, G. Impact of Energy Filtering and Carrier Localization on the Thermoelectric Properties of Granular Semiconductors. *J. Solid State Chem.* **2012**, *193*, 19−25.

(6) Kovalenker, V. A. Mohite, Cu_2SnS_3, a New Sulfide of Tin and Copper. *Int. Geol. Rev.* **1983**, *25*, 117−120.

(7) Wei, Y.; Zhou, Z.; Jiang, P.; Zheng, S.; Xiong, Q.; Zhang, B.; Wang, G.; Lu, X.; Han, G.; Zhou, X. Phase Composition

Manipulation and Twin Boundary Engineering Lead to Enhanced Thermoelectric Performance of Cu_2SnS_3. *ACS Appl. Energy Mater.* **2021**, *4*, 9240−9247.
(8) Nautiyal, H.; Lohani, K.; Mukherjee, B.; Isotta, E.; Malagutti, M. A.; Ataollahi, N.; Pallecchi, I.; Putti, M.; Misture, S. T.; Rebuffi, L.; Scardi, P. Mechanochemical Synthesis of Sustainable Ternary and Quaternary Nanostructured Cu_2SnS_3, Cu_2ZnSnS_4, and $Cu_2ZnSnSe_4$ Chalcogenides for Thermoelectric Applications. *Nanomaterials* **2023**, No. 366.
(9) Koskela, K. M.; Mora Perez, C.; Eremin, D. B.; Evans, J. M.; Strumolo, M. J.; Lewis, N. S.; Prezhdo, O. V.; Brutchey, R. L. Polymorphic Control of Solution-Processed Cu_2SnS_3 Films with Thiol−Amine Ink Formulation. *Chem. Mater.* **2022**, *34*, 8654−8663.
(10) Syafiq, U.; Isotta, E.; Ataollahi, N.; Lohani, K.; Luong, S.; Trifiletti, V.; Fenwick, O.; Scardi, P. Facile and Low-Cost Fabrication of Cu/Zn/Sn-Based Ternary and Quaternary Chalcogenides Thermoelectric Generators. *ACS Appl. Energy Mater.* **2022**, *5*, 5909−5918.
(11) Lohani, K.; Nautiyal, H.; Ataollahi, N.; Fanciulli, C.; Sergueev, I.; Etter, M.; Scardi, P. Experimental and *Ab Initio* Study of Cu_2SnS_3 (CTS) Polymorphs for Thermoelectric Applications. *J. Phys. Chem. C* **2021**, *125*, 178−188.
(12) Hu, L.; Luo, Y.; Fang, Y. W.; Qin, F.; Cao, X.; Xie, H.; Liu, J.; Dong, J.; Sanson, A.; Giarola, M.; Tan, X.; Zheng, Y.; Suwardi, A.; Huang, Y.; Hippalgaonkar, K.; He, J.; Zhang, W.; Xu, J.; Yan, Q.; Kanatzidis, M. G. High Thermoelectric Performance through Crystal Symmetry Enhancement in Triply Doped Diamondoid Compound Cu_2SnSe_3. *Adv. Energy Mater.* **2021**, *11*, No. 2100661.
(13) Zhang, D.; Zhang, B.; Zhou, Z.; Peng, K.; Wu, H.; Wang, H.; Wang, G.; Han, G.; Wang, G.; Zhou, X.; Lu, X. Ultralow Lattice Thermal Conductivity of Cubic $CuFeS_2$ Induced by Atomic Disorder. *Chem. Mater.* **2021**, *33*, 9795.
(14) Zhai, H.; Xiao, Y.; Zhao, L.-D.; Tan, G.; Tang, X. Large Effective Mass and Low Lattice Thermal Conductivity Contributing to High Thermoelectric Performance of Zn-Doped $Cu_5Sn_2Se_7$. *J. Alloys Compd.* **2020**, *826*, No. 154154.
(15) Deng, T.; Qiu, P.; Xing, T.; Zhou, Z.; Wei, T. R.; Ren, D.; Xiao, J.; Shi, X.; Chen, L. A Low-Cost and Eco-Friendly Br-Doped $Cu_7Sn_3S_{10}$ Thermoelectric Compound With zT around Unity. *J. Mater. Chem. A* **2021**, *9*, 7946−7954.
(16) Isotta, E.; Mukherjee, B.; Bette, S.; Dinnebier, R.; Scardi, P. Static and Dynamic Components of Debye−Waller Coefficients in the Novel Cubic Polymorph of Low-Temperature Disordered Cu_2ZnSnS_4. *IUCrJ* **2022**, *9*, 272−285.
(17) Isotta, E.; Mukherjee, B.; Fanciulli, C.; Ataollahi, N.; Sergueev, I.; Stankov, S.; Edla, R.; Pugno, N. M.; Scardi, P. Origin of a Simultaneous Suppression of Thermal Conductivity and Increase of Electrical Conductivity and Seebeck Coefficient in Disordered Cubic Cu_2ZnSnS_4. *Phys. Rev. Appl.* **2020**, *14*, No. 064073.
(18) Ataollahi, N.; Bazerla, F.; Malerba, C.; Chiappini, A.; Ferrari, M.; Di Maggio, R.; Scardi, P. Synthesis and Post-Annealing of Cu_2ZnSnS_4 Absorber Layers Based on Oleylamine/1-Dodecanethiol. *Materials* **2019**, *12*, No. 3320.
(19) Zhao, Q.; Qin, B.; Wang, D.; Qiu, Y.; Zhao, L. D. Realizing High Thermoelectric Performance in Polycrystalline SnSe via Silver Doping and Germanium Alloying. *ACS Appl. Energy Mater.* **2020**, *3*, 2049−2054.
(20) Sharma, S. D.; Khasimsaheb, B.; Chen, Y. Y.; Neeleshwar, S. Enhanced Thermoelectric Performance of Cu_2ZnSnS_4 (CZTS) by Incorporating Ag Nanoparticles. *Ceram. Int.* **2019**, *45*, 2060−2068.
(21) Ballikaya, S.; Chi, H.; Salvador, J. R.; Uher, C. Thermoelectric Properties of Ag-Doped Cu_2Se and Cu_2Te. *J. Mater. Chem. A* **2013**, *1*, 12478.
(22) Zhang, L.; Wang, J.; Cheng, Z.; Sun, Q.; Li, Z.; Dou, S. Lead-Free SnTe-Based Thermoelectrics: Enhancement of Thermoelectric Performance by Doping with Gd/Ag. *J. Mater. Chem. A* **2016**, *4*, 7936−7942.
(23) Jin, Z.; Mao, T.; Qiu, P.; Yue, Z.; Wang, L.; Zhao, K.; Ren, D.; Shi, X.; Chen, L. Thermoelectric Properties and Service Stability of Ag-Containing Cu_2Se. *Mater. Today Phys.* **2021**, *21*, No. 100550.
(24) Cheng, X.; Yang, D.; Su, X.; Xie, H.; Liu, W.; Zheng, Y.; Tang, X. Synergistically Enhanced Thermoelectric Performance of Cu_2SnSe_3-Based Composites via Ag Doping Balance. *ACS Appl. Mater. Interfaces* **2021**, *13*, 55178−55187.
(25) Mehmood, F.; Wang, H.; Su, W.; Khan, M.; Huo, T.; Chen, T.; Chebanova, G.; Romanenko, A.; Wang, C. Enhanced Power Factor and Figure of Merit of $Cu_2ZnSnSe_4$-Based Thermoelectric Composites by Ag Alloying. *Inorg. Chem.* **2021**, *60*, 3452−3459.
(26) Lohani, K.; Nautiyal, H.; Ataollahi, N.; Maji, K.; Guilmeau, E.; Scardi, P. Effects of Grain Size on the Thermoelectric Properties of Cu_2SnS_3: An Experimental and First-Principles Study. *ACS Appl. Energy Mater.* **2021**, *4*, 12604−12612.
(27) Isotta, E.; Fanciulli, C.; Pugno, N. M.; Scardi, P. Effect of the Order-Disorder Transition on the Seebeck Coefficient of Nanostructured Thermoelectric Cu_2ZnSnS_4. *Nanomaterials* **2019**, *9*, No. 762.
(28) Mukherjee, B.; Isotta, E.; Malagutti, M. A.; Lohani, K.; Rebuffi, L.; Fanciulli, C.; Scardi, P. Thermoelectric Performance in Disordered $Cu_2ZnSnSe_4$ Nanostructures Driven by Ultra-Low Thermal Conductivity. *J. Alloys Compd.* **2023**, *933*, No. 167756.
(29) Ming, H.; Zhu, G.; Zhu, C.; Qin, X.; Chen, T.; Zhang, J.; Li, D.; Xin, H.; Jabar, B. Boosting Thermoelectric Performance of Cu_2SnSe_3 via Comprehensive Band Structure Regulation and Intensified Phonon Scattering by Multidimensional Defects. *ACS Nano* **2021**, *15*, 10532−10541.
(30) McCusker, L. B.; Von Dreele, R. B.; Cox, D. E.; Louër, D.; Scardi, P. Rietveld Refinement Guidelines. *J. Appl. Cryst.* **1999**, *32*, 36−50.
(31) Scardi, P. Diffraction Line Profiles in the Rietveld Method. *Cryst. Growth Des.* **2020**, *20*, 6903−6916.
(32) Scardi, P. Microstructural Properties: Lattice Defects and Domain Size Effects. *Powder Diffraction*; Royal Society of Chemistry: Cambridge, 2008; Chapter 13, pp 376−413, DOI: 10.1039/9781847558237-00376.
(33) Scardi, P.; Azanza Ricardo, C. L.; Perez-Demydenko, C.; Coelho, A. A. Whole Powder Pattern Modelling Macros for TOPAS. *J. Appl. Cryst.* **2018**, *51*, 1752−1765.
(34) Coelho, A. A. TOPAS and TOPAS-Academic: An Optimization Program Integrating Computer Algebra and Crystallographic Objects Written in C++. *J. Appl. Cryst.* **2018**, *51*, 210−218.
(35) Kresse, G.; Furthmüller, J. Efficiency of Ab-Initio Total Energy Calculations for Metals and Semiconductors Using a Plane-Wave Basis Set. *Comput. Mater. Sci.* **1996**, *6*, 15−50.
(36) Kresse, G.; Furthmüller, J. Efficient Iterative Schemes for Ab Initio Total-Energy Calculations Using a Plane-Wave Basis Set. *Phys. Rev. B* **1996**, *54*, 11169.
(37) Perdew, J. P.; Burke, K.; Ernzerhof, M. Generalized Gradient Approximation Made Simple. *Phys. Rev. Lett.* **1996**, *77*, 3865−3868.
(38) Heyd, J.; Scuseria, G. E. Efficient Hybrid Density Functional Calculations in Solids: Assessment of the Heyd-Scuseria-Ernzerhof Screened Coulomb Hybrid Functional. *J. Chem. Phys.* **2004**, *121*, 1187−1192.
(39) Togo, A.; Tanaka, I. First Principles Phonon Calculations in Materials Science. *Scr. Mater.* **2015**, *108*, 1−5.
(40) Zhao, H.; Xu, X.; Li, C.; Tian, R.; Zhang, R.; Huang, R.; Lyu, Y.; Li, D.; Hu, X.; Pan, L.; Wang, Y. Cobalt-Doping in Cu_2SnS_3: Enhanced Thermoelectric Performance by Synergy of Phase Transition and Band Structure Modification. *J. Mater. Chem. A* **2017**, *5*, 23267−23275.
(41) Zhou, W.; Dwivedi, P.; Shijimaya, C.; Ito, M.; Higashimine, K.; Nakada, T.; Takahashi, M.; Mott, D.; Miyata, M.; Ohta, M.; Miwa, H.; Akatsuka, T.; Maenosono, S. Enhancement of the Thermoelectric Figure of Merit in Blended $Cu_2Sn_{1-x}Zn_xS_3$ Nanobulk Materials. *ACS Appl. Nano Mater.* **2018**, *1*, 4819−4827.
(42) Shen, Y.; Li, C.; Huang, R.; Tian, R.; Ye, Y.; Pan, L.; Koumoto, K.; Zhang, R.; Wan, C.; Wang, Y. Eco-Friendly p-Type Cu_2SnS_3 Thermoelectric Material: Crystal Structure and Transport Properties. *Sci. Rep.* **2016**, *6*, No. 32501.

(43) Zhang, Z.; Zhao, H.; Wang, Y.; Hu, X.; Lyu, Y.; Cheng, C.; Pan, L.; Lu, C. Role of Crystal Transformation on the Enhanced Thermoelectric Performance in Mn-Doped Cu_2SnS_3. *J. Alloys Compd.* **2019**, *780*, 618−625.
(44) Lohani, K.; Fanciulli, C.; Scardi, P. Effects of Preparation Procedures and Porosity on Thermoelectric Bulk Samples of Cu_2SnS_3 (CTS). *Materials* **2022**, *15*, No. 712.
(45) Deng, T.; Qiu, P.; Song, Q.; Chen, H.; Wei, T.-R.; Xi, L.; Shi, X.; Chen, L. Thermoelectric Properties of Non-Stoichiometric $Cu_{2+x}Sn_{1-x}S_3$ Compounds. *J. Appl. Phys.* **2019**, *126*, No. 085111.
(46) Snyder, G. J.; Snyder, A. H.; Wood, M.; Gurunathan, R.; Snyder, B. H.; Niu, C. Weighted Mobility. *Adv. Mater.* **2020**, *32*, No. 2001537.
(47) Xie, H.; Su, X.; Hao, S.; Zhang, C.; Zhang, Z.; Liu, W.; Yan, Y.; Wolverton, C.; Tang, X.; Kanatzidis, M. G. Large Thermal Conductivity Drops in the Diamondoid Lattice of $CuFeS_2$ by Discordant Atom Doping. *J. Am. Chem. Soc.* **2019**, *141*, 18900−18909.
(48) Li, Y.; Liu, G.; Cao, T.; Liu, L. M.; Li, J.; Chen, K.; Li, L.; Han, Y.; Zhou, M. Enhanced Thermoelectric Properties of Cu_2SnSe_3 by (Ag,In)-Co-Doping. *Adv. Funct. Mater.* **2016**, *26*, 6025−6032.
(49) Zhao, L.; Chen, C.; Pan, L.; Hu, X.; Lu, C.; Wang, Y. Magnetic Iron Doping in Cu_2SnS_3 Ceramics for Enhanced Thermoelectric Transport Properties. *J. Appl. Phys.* **2019**, *125*, No. 095107.
(50) Siyar, M.; Cho, J. Y.; Youn, Y.; Han, S.; Kim, M.; Bae, S. H.; Park, C. Effect of Annealing Temperature on the Phase Transition, Band Gap and Thermoelectric Properties of Cu_2SnSe_3. *J. Mater. Chem. C* **2018**, *6*, 1780−1788.
(51) Baláž, P.; Achimovičová, M.; Baláž, M.; Chen, K.; Dobrozhan, O.; Guilmeau, E.; Hejtmánek, J.; Knížek, K.; Kubíčková, L.; Levinský, P.; Puchý, V.; Reece, M. J.; Varga, P.; Zhang, R. Thermoelectric Cu−S-Based Materials Synthesized via a Scalable Mechanochemical Process. *ACS Sustainable Chem. Eng.* **2021**, *9*, 2003−2016.
(52) Yang, Y.; Ying, P.; Wang, J.; Liu, X.; Du, Z.; Chao, Y.; Cui, J. Enhancing the Thermoelectric Performance of Cu_3SnS_4-Based Solid Solutions through Coordination of the Seebeck Coefficient and Carrier Concentration. *J. Mater. Chem. A* **2017**, *5*, 18808−18815.
(53) Kumar, V. P.; Lemoine, P.; Carnevali, V.; Guélou, G.; Lebedev, O. I.; Raveau, B.; Al Rahal Al Orabi, R.; Fornari, M.; Candolfi, C.; Prestipino, C.; Menut, D.; Malaman, B.; Juraszek, J.; Suekuni, K.; Guilmeau, E. Local-Disorder-Induced Low Thermal Conductivity in Degenerate Semiconductor $Cu_{22}Sn_{10}S_{32}$. *Inorg. Chem.* **2021**, *60*, 16273−16285.
(54) Kim, H.-S.; Gibbs, Z. M.; Tang, Y.; Wang, H.; Snyder, G. J. Characterization of Lorenz Number with Seebeck Coefficient Measurement. *APL Mater.* **2015**, *3*, No. 041506.
(55) Liu, W.; Shi, X.; Hong, M.; Yang, L.; Moshwan, R.; Chen, Z. G.; Zou, J. Ag Doping Induced Abnormal Lattice Thermal Conductivity in Cu_2Se. *J. Mater. Chem. C* **2018**, *6*, 13225−13231.
(56) Cao, L.; Du, X.; Guo, X.; Yuan, Z. The Enhanced Electrical Transport Properties of Fe^{3+} Doped Cu_2SnS_3. *Electron. Mater. Lett.* **2021**, *17*, 493−499.
(57) Tan, Q.; Sun, W.; Li, Z.; Li, J. F. Enhanced Thermoelectric Properties of Earth-Abundant Cu_2SnS_3 via In Doping Effect. *J. Alloys Compd.* **2016**, *672*, 558−563.
(58) Xu, X.; Zhao, H.; Hu, X.; Pan, L.; Chen, C.; Li, D.; Wang, Y. Synergistic Role of Ni-Doping in Electrical and Phonon Transport Properties of $Cu_2Sn_{1-x}Ni_xS_3$. *J. Alloys Compd.* **2017**, *728*, 701−708.
(59) Zhao, Y.; Gu, Y.; Zhang, P.; Hu, X.; Wang, Y.; Zong, P.; Pan, L.; Lyu, Y.; Koumoto, K. Enhanced Thermoelectric Performance in Polymorphic Heavily Co-Doped Cu_2SnS_3 through Carrier Compensation by Sb Substitution. *Sci. Technol. Adv. Mater.* **2021**, *22*, 363−372.
(60) Xing, W.; Zhao, Z.; Pan, L.; Chen, C.; Li, D.; Wang, Y. Thermoelectric Properties and Magnetoelectric Coupling in Dually Doped $Cu_2Sn_{1-2x}Zn_xFe_xS_3$. *J. Mater. Sci.: Mater. Electron.* **2020**, *31*, 11801−11809.
(61) Li, C.; Song, H.; Cheng, Y.; Qi, R.; Huang, R.; Cui, C.; Wang, Y.; Zhang, Y.; Miao, L. Highly Suppressed Thermal Conductivity in Diamond-like Cu_2SnS_3 by Dense Dislocation. *ACS Appl. Energy Mater.* **2021**, *4*, 8728−8733.
(62) Gu, Y.; Ai, W.; Zhao, Y.; Hu, X.; Pan, L.; Zong, P.; Lu, C.; Xu, Z.; Wang, Y. Remarkable Thermoelectric Property Enhancement in Cu_2SnS_3-$CuCo_2S_4$ Nanocomposites via 3D Modulation Doping. *J. Mater. Chem. A* **2021**, *9*, 16928−16935.
(63) Kim, S.; Hwang, J.; You, T.-S.; Yeon, S.; Kim, J.; Yu, B.-K.; Han, M.-K.; Lee, M.; Acharya, S.; Kim, J.; Kim, W.; Kim, S.-J. Enhanced Thermoelectric Performance by Resonant Doping and Embedded Magnetic Impurity. *Phys. Rev. Appl.* **2023**, *19*, No. 014034.

https://doi.org/10.1021/acsanm.3c00716
ACS Appl. Nano Mater. 2023, 6, 6323−6333